Magnetic Resonance in Medicine 48:1011–1020 (2002)

# Application of Sensitivity-Encoded Echo-Planar Imaging for Blood Oxygen Level-Dependent Functional Brain Imaging

Jacco A. de Zwart,[1]* Peter van Gelderen,[1] Peter Kellman,[2] and Jeff H. Duyn[1]

**The benefits of sensitivity-encoded (SENSE) echo-planar imaging (EPI) for functional MRI (fMRI) based on blood oxygen level-dependent (BOLD) contrast were quantitatively investigated at 1.5 T. For experiments with 3.4 × 3.4 × 4.0 mm$^3$ resolution, SENSE allowed the single-shot EPI image acquisition duration to be shortened from 24.1 to 12.4 ms, resulting in a reduced sensitivity to geometric distortions and $T_2^*$ blurring. Finger-tapping fMRI experiments, performed on eight normal volunteers, showed an overall 18% loss in *t*-score in the activated area, which was substantially smaller than expected based on the image signal-to-noise ratio (SNR) and *g*-factor, but similar to the loss predicted by a model that takes physiologic noise into account. Magn Reson Med 48:1011–1020, 2002. Published 2002 Wiley-Liss, Inc.†**

**Key words: MRI; accelerated imaging; SENSE; brain imaging; fMRI; BOLD**

Functional magnetic resonance imaging (fMRI) studies based on blood oxygen level-dependent (BOLD) contrast require rapid scan techniques that are robust under conditions such as subject motion and tissue pulsations. This is because the signal changes due to neuronal activation are only a small percentage of the full MRI signal, and thus are difficult to distinguish from other signal fluctuations.

In fMRI, single-shot techniques such as echo-planar imaging (EPI) and spiral imaging are often preferred over multishot techniques because of their reduced sensitivity for shot-to-shot signal variations (1,2). However, these techniques require rapid gradient switching, leading to high levels of acoustic noise and potentially to peripheral nerve stimulation. In addition, image quality is affected by blurring and warping, caused by $T_2^*$ and off-resonance effects. These effects increase with $B_0$-field strength and limit the achievable spatial resolution.

With single-shot EPI techniques, blurring can be reduced by using reduced data acquisition techniques, such as half *k*-space acquisition, combined with homodyne image reconstruction (3,4). These techniques appear to have some benefits for fMRI (5), although they can potentially lead to image artifacts caused by errors in background phase.

One way to reduce both blurring and warping in single-shot fMRI would be to combine EPI with recently introduced parallel imaging techniques (6–9), which allow reconstruction of undersampled MR data. These techniques exploit the spatial differences in sensitivity profiles of the individual channels in detector arrays (10) to reconstruct MR images from reduced field-of-view (FOV) data (6). For a given resolution, this undersampling strategy could be used to reduce image artifacts by shortening the data acquisition window (e.g., geometrical distortions (11)) or to reduce gradient switching rates (12). Although parallel imaging techniques show great promise in applications such as cardiac imaging (13–15), angiography (16), and diffusion-weighted imaging (11), the benefit for single-shot fMRI has not yet been demonstrated. A preliminary application of SENSE to multishot fMRI showed that a twofold increase in scan speed can be achieved at a relatively small (~20%) reduction in signal stability (17). However, the effect of SENSE on the statistical power (*t*-score per unit scan time) in fMRI was not quantified.

In the following, the fMRI sensitivity of SENSE single-shot EPI and conventional single-shot EPI are compared quantitatively. The *t*-score penalty incurred with SENSE is compared to the *t*-score penalty predicted on the basis of relative contribution of intrinsic and physiological noise. Finger-tapping experiments performed on normal volunteers are used to investigate various undersampling strategies to increase image acquisition speed.

## MATERIALS AND METHODS

### Background

Parallel imaging MRI techniques achieve undersampling by reduction of the FOV in one or more spatial directions. With appropriate detector arrays, these can include the image-encoding axes (8,9), or the slice-select direction (18). The aliasing artifacts associated with undersampling are cancelled by applying dedicated postprocessing methods, which incorporate knowledge about differences in the spatially varying sensitivity profiles of the various receive coil channels. These coil sensitivity reference data can be collected in a separate experiment using a volume RF coil with a uniform reception profile (9), or derived from the undersampled data itself using a limited number additional *k*-space lines (19). In repetitive scanning, reference data can be derived by temporal shifting of acquired *k*-space lines in an interleaved manner, thus acquiring the full *k*-space when combining data from different time points (referred to as TSENSE) (20). The adaptive derivation of coil sensitivity maps from the actual data (self calibration) has the potential advantage of being able to accommodate changes in position of the subject and/or coil elements over the course of the experiment.

The application of SENSE introduces spatially varying noise amplification (loss in signal-to-noise ratio (SNR))

[1]Advanced MRI, Laboratory of Functional and Molecular Imaging, NINDS, National Institutes of Health, Bethesda, Maryland. [2]Laboratory of Cardiac Energetics, NHLBI, National Institutes of Health, Bethesda, Maryland.

*Correspondence to: Jacco de Zwart, Advanced MRI, LFMI, NINDS, National Institutes of Health, Bldg. 10, Rm. B1D-118, 10 Center Dr., Bethesda, MD 20892-1065. E-mail: Jacco.deZwart@nih.gov

Received 27 November 2001; revised 24 July 2002; accepted 1 August 2002.

DOI 10.1002/mrm.10303

Published online in Wiley InterScience (www.interscience.wiley.com).

depending on the orthogonality of the sensitivity profiles of the individual coil channels. This noise amplification has been described in the literature and can be characterized by the so-called "geometry" factor $g$ (9). This factor is determined by sensitivity differences between the coils for the sample regions that are superimposed in the aliased image. Generally speaking, the $g$-factors increase with increasing undersampling rate, $R$, and decrease with increasing number of detector channels (21). When SENSE is applied to shorten the image acquisition window, an additional loss in image SNR is incurred due to sampling time reduction, which is proportional to the square root of the fractional shortening, i.e., $\sqrt{R}$, leading to a total SENSE-related SNR loss of $g \cdot \sqrt{R}$ (9).

The effect of this SENSE-related SNR loss on the sensitivity in BOLD fMRI is not directly evident because of the added contribution of physiological noise. The sensitivity in BOLD fMRI scales with stability of the image intensity time course, which is determined by a combination of intrinsic image SNR and physiological noise levels. The use of SENSE will reduce the intrinsic image SNR, whereas no significant effect on physiological noise is expected. Therefore, the penalty for applying SENSE in fMRI will depend on the relative contribution of intrinsic image variance to the overall temporal variance. In cases in which temporal stability is fully determined by the intrinsic noise (e.g., resulting from thermal noise sources), an fMRI sensitivity penalty of $g \cdot \sqrt{R}$ is expected when using SENSE EPI instead of conventional EPI. On the other hand, when physiological instabilities (e.g., due to patient motion, respiration, and blood/tissue pulsation) are predominant, the penalty incurred with SENSE acceleration is expected to reduce from a factor $g \cdot \sqrt{R}$ to 1. A more detailed description of the noise behavior of SENSE data is given in Appendix A. The losses encountered in practice will depend strongly on experimental conditions. For example, estimating coil sensitivity profiles in the presence of subject motion might be less accurate.

The experiments described below were designed to investigate these issues. The sensitivity of BOLD fMRI with application of rate-2 SENSE-EPI for shortening of the data acquisition window was investigated using a four-element receive-only array. The statistical significance of the detected BOLD signal changes in the primary motor cortex (PMC), expressed by Student's $t$-score, was compared for SENSE and conventional EPI BOLD fMRI data, acquired with identical spatial resolution in the same session on the same volunteers.

### MRI Hardware

Experiments were performed on a GE Signa LX scanner (General Electric Company, Milwaukee, WI) with four receive channels, each with 250 kHz bandwidth. The maximum gradient strength and slew rate were 50 $mT \cdot m^{-1}$ and 180 $T \cdot m^{-1} \cdot s^{-1}$, respectively. For all experiments, a prototype, four-element, dome-shaped array coil (Nova Medical Inc., Wakefield, MA) was used (Fig. 1a), which employs a gapped-element design (18). The surface of each trapezoidal element was approximately 100 $cm^2$ (elements were 14 cm in length, and width varied from approximately 4 cm on top to 11 cm near the rim of the coil). The gap between elements ranged from 2.5 cm at the superior to 7.5 cm at the inferior boundary of the array coil. The diameter of the array coil, at the inferior rim, was 26 cm. To minimize coupling between the coil elements, dedicated high-impedance preamplifiers (22) (model NMP-1; Nova Medical Inc., Wakefield, MA) were used, which had a nominal input impedance of 2 kΩ. The resulting coupling between the coil elements was estimated to be below 5%. Figure 1b shows images obtained in parallel from each of the four elements of the array coil, illustrating the individual profiles and the absence of obvious coupling effects. In most brain regions, SNR in optimally combined images (see Appendix B), obtained with this coil (Fig. 1c, top row), was superior to that obtained with the 29-cm-diameter product birdcage head resonator (model 46-28211186202; GE Medical, Milwaukee, WI) (Fig. 1c, bottom row). Using the array coil, the SNR in peripheral brain regions in the superior brain was close to threefold higher than with the product coil. With the coil elements placed in the anterior, right, posterior, and left positions (12, 3, 6, and 9 o'clock positions in Fig. 1b and c), the highest SENSE $g$-values were found in the most anterior and posterior brain regions (see Fig. 1d).

### EPI Scanning

An in-house-developed EPI sequence was used, which employed sampling on the ramps of the read-out gradient, used maximum gradient slew-rates of 150 $T \cdot m^{-1} \cdot s^{-1}$, and acquired one extra $k$-space reference line to correct for phase difference between odd and even echoes (23). Fifty percent of the read-out gradient ramp was used for the acquisition of data using 4 μs dwell time (250 kHz acquisition bandwidth). The alternating read-out gradient was applied in the anterior-posterior ($y$) direction. To reconstruct the image using the data acquired during ramping of the read-out gradient, a Fourier transform with nonlinear sampling was applied to convert data from $k$-space to image space.

### fMRI Protocol

Conventional and rate-2 SENSE EPI acquisitions were performed during a sequential finger-tapping activation paradigm, visually paced at two taps $\cdot$ $s^{-1}$ (2 Hz). The scans were performed in random order on normal volunteers (males and females; $N = 8$), ranging in age from 23.4 to 43.2 years (31.4 years on average). All scans were performed with informed consent in accordance with an NIH-approved protocol (IRB approval number: 00-N-0082; last reviewed March 29, 2002). Twelve axial slices were recorded in the superior brain, with a 1-mm gap, using an overall TR of 2000 ms, TE of 40 ms, and flip angle of 90°.

### fMRI With Shortened EPI Data Acquisition Window

To evaluate the effects of shortening the acquisition window in EPI fMRI using SENSE, conventional full-FOV EPI (Fig. 2a, *full*) was compared with rate-2 SENSE EPI with an approximately 50% window shortening (Fig. 2b and c). Two different SENSE strategies were used: one in which the coil sensitivity maps were derived exclusively from data acquired prior to the fMRI run (*SENSE-odd*, Fig. 2b), and one in which these data were acquired over the course of the experiment (*SENSE-alt*, also known as TSENSE

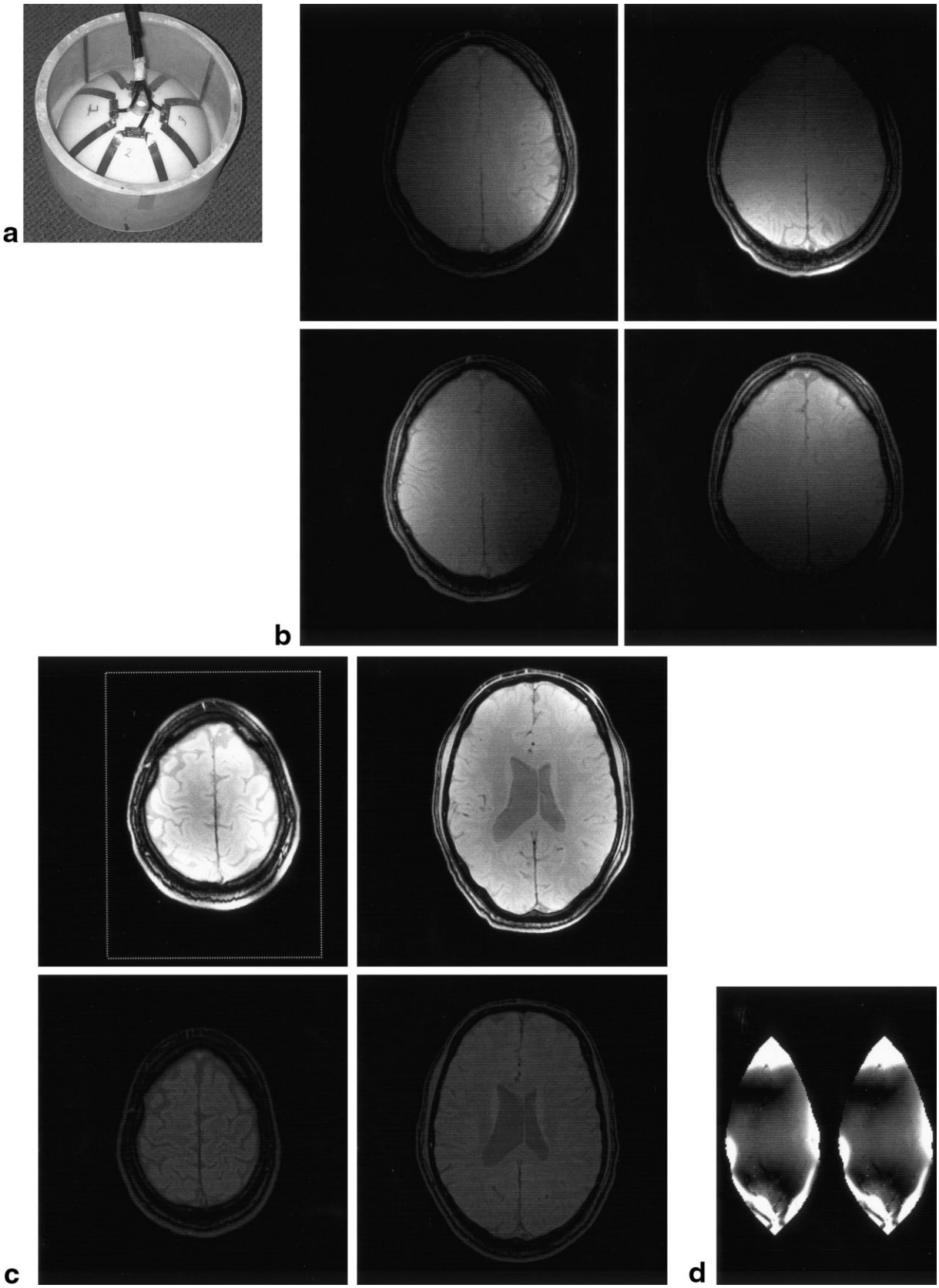


FIG. 1. A four-channel RF receive coil array was used in all experiments. **a:** Layout of conductors on the former. Four triangle-shaped coil elements were positioned on a spherical former. The gaps between the elements varied from approximately 2.5 cm at the top to 7.5 cm at the bottom. **b:** Brain images from individual coil channels. Note the independence of the profiles. Coupling between any pair of elements was below 5%. **c:** Brain coverage of the four-channel coil array. Shown are SNR maps of the optimally combined coil signals for two axial slices through the superior brain (top row). Comparative images recorded with a conventional quadrature birdcage coil on the same volunteer in the same session are shown in the bottom row. All four images are scaled from an SNR of 0 (black) to an SNR $\geq$ 200 (white). The region within the rectangle in the top left image corresponds to the FOV used in the EPI experiments (220 $\times$ 165 $mm^2$). **d:** Map of *g*-values computed from individual coil data for the area within the rectangle in the top left slice of **c**.

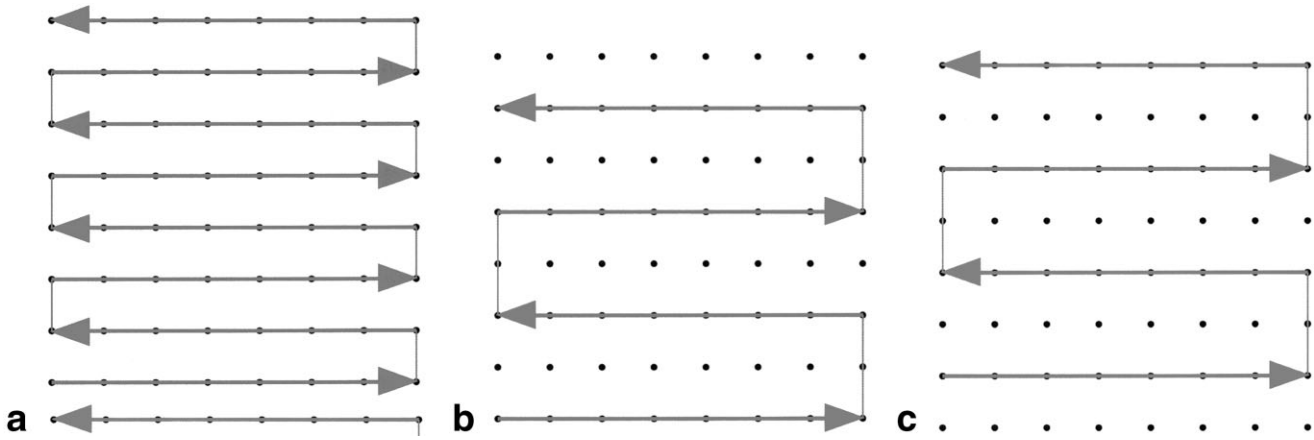


FIG. 2. Schematic display of the *k*-space strategies used in the BOLD fMRI experiments. Single-shot EPI was performed (**a**) with full coverage of *k*-space, (**b**) with acquisition of only the odd-numbered *k*-space lines, or with acquisition of alternately (**b**) odd- and (**c**) even-numbered *k*-space lines.

(20)). In *SENSE-odd*, only the odd-numbered *k*-space lines were acquired during the fMRI run, whereas in *SENSE-alt*, alternately the odd- and even-numbered *k*-space lines were acquired on successive time points (repetitive alternation of Fig. 2b and c). The latter strategy allowed calculation of relative coil sensitivity maps (reference data) during the entire fMRI time-series by combining *k*-space data from successive time points (20), with the potential advantage of improved robustness in the presence of motion-related changes in coil sensitivities. To obtain coil sensitivity data for the *SENSE-odd* data, an additional 20-s (10-volume) initial (rest) period was inserted at the beginning of each fMRI run, during which time data was acquired with the *SENSE-alt* strategy. The first four time points of each run, which showed intensity variations due to approach to steady state, were discarded, leaving six time points for reference data for *SENSE-odd*. This amount of data provided adequate SNR for determination of coil sensitivity profiles, as evidenced by the fact that lengthening the initial rest period to 60 s (26 time points for reference data) did not significantly alter the fMRI results (data not shown). For *SENSE-alt*, both initial rest data and data acquired during the actual fMRI run were averaged to obtain sensitivity maps.

For comparison, SENSE-like data were also synthesized from the *full* fMRI run by selectively discarding *k*-space lines, referred to as *syn-alt* and *syn-odd*. Both *SENSE-alt* and *SENSE-odd* were then compared with these synthetic *syn-alt* and *syn-odd* data.

For the *full* run, an FOV of 220 × 165 $mm^2$ (anterior–posterior × left–right) was chosen to narrowly fit the head in the most inferior of the selected slices. The EPI matrix size was 64 × 48, resulting in a nominal in-plane resolution of 3.44 mm. The slice thickness was 4 mm. The SENSE experiments were performed with 220 × 83 $mm^2$ FOV and 64 × 24 matrix size. Total duration of the readout window (EPI train length) was 24.1 ms for conventional EPI and 12.4 ms for SENSE EPI, resulting in sensitivities to off-resonance-related geometric distortions of 83 and 43 $\mu m \cdot Hz^{-1}$, respectively.

### Image Reconstruction

Unless otherwise stated, image reconstruction and data analysis were performed off-line using in-house-developed code for IDL software (Research Systems Inc., Boulder, CO). Coil sensitivity profiles were calculated in each fMRI run by taking the average of the image time-series, as was described above. Subsequently, phase and intensity contrast related to the object were removed, and polynomial fitting was used to estimate the coil sensitivity in the vicinity of the object edge (see Appendix C). The resulting sensitivity profiles did not represent absolute coil sensitivities, but rather sensitivity values relative to the other coils.

Using the sensitivity matrix **S**, the combined image values $I_c$ were then computed on a pixel-by-pixel basis from coil image values **P** (9):

$$I_c = (\mathbf{S}^H \boldsymbol{\Psi}^{-1} \mathbf{S})^{-1} \mathbf{S}^H \boldsymbol{\Psi}^{-1} \mathbf{P} \quad [1]$$

where $\boldsymbol{\Psi}$ is the noise covariance matrix (see Appendix D). SENSE *g*-factors (9) were calculated using:

$$g_q = \sqrt{(\mathbf{S}^H \boldsymbol{\Psi}^{-1} \mathbf{S})^{-1}_{q,q} (\mathbf{S}^H \boldsymbol{\Psi}^{-1} \mathbf{S})_{q,q}}. \quad [2]$$

Note that in the case of SENSE acquisition, **P** consisted of aliased pixel values. In the case of full *k*-space (full-FOV) reconstruction, **S** was a vector with the four coil sensitivities in the pixel under consideration, whereas in SENSE reconstruction, **S** had an extra dimension containing the coil sensitivities in the aliased areas. The index $q$ in Eq. [2] refers to the $q$th image region, where $q$ ranges from 1 to $R$. This reconstruction led to a sensitivity-optimized combination of coil channels and minimal aliasing. However, due to the nature of the sensitivity profiles, i.e., the lack of absolute sensitivities, the reconstructed image intensity was nonuniform, and not representative of local SNR. The latter was calculated using additional analysis as described in Appendix B.

### Statistical Analysis

To evaluate the sensitivity of the full *k*-space and SENSE fMRI runs, statistical analysis was performed on the time-series data. For this purpose, multilinear regression was performed using four regressors: the stimulus function convolved with a hemodynamic response function, baseline intensity, linear drift, and a "saw-tooth" function describing the possible signal intensity fluctuations in *SENSE-alt* and *syn-alt* runs that are related to the different *k*-space trajectories used in subsequent images. Note that for consistency of the data analysis, the saw-tooth regressor was also used when *SENSE-odd*, *syn-odd*, and *full* data were analyzed, even though such a signal fluctuation is not present there. Since the frequency of this function is 15-fold higher than the frequency of the activation paradigm, it is not expected to have a significant effect on the detection of activation. The hemodynamic response function was modeled as a truncated Gaussian function ($\sigma$ = 3.5 s, 5 s delayed) (24). The regression analysis returned statistical *t*-scores, as well as the standard deviation (SD) of the difference between data and fit, expressed as a percentage of the baseline image intensity. This SD was used as a measure of temporal noise of the image intensity time course, in the following referred to as relative temporal SD $\sigma_t$. For each subject, a single region-of-interest (ROI) in the PMC area was selected, based on anatomy. Voxels within this ROI, and with *t*-values above 4.5 in any of the runs, were used to generate a "functional" PMC (FPMC) ROI, over which *t*-scores and $\sigma_t$ values were averaged. To estimate the contribution of thermal noise to $\sigma_t$, thermal (intrinsic) noise levels, normalized to image signal intensity, ($\sigma_i$) were derived from full-FOV data (see Appendix B). For comparison, $\sigma_i$ and $\sigma_t$ levels were also derived over a larger ROI, which includes the entire superior brain (SB). Only slices that contributed at least one voxel to the PMC ROI were included in SB.

Since FPMC selection was based on the functional data itself, it potentially introduced a bias favoring the experiment with the largest number of significantly activated voxels. In order to estimate the magnitude of this bias, additional analysis was performed using an alternative selection of functional PMC. This was done by selecting only voxels with significant activation in all experiments. This ROI, referred to as FPMC2, had an opposite selection bias, favoring the experiment with the lowest sensitivity for activated voxels. Differences between the results of analyses with FPMC and FPMC2 ROI's would therefore indicate the severity of the bias. Alternatively, selection bias could be avoided altogether by using an anatomy-based ROI; however, this would substantially reduce the sensitivity of the comparison.

To investigate the influence of physiological noise sources on SENSE fMRI performance, the increase in $\sigma_t$ with SENSE as a function of the ratio of $\sigma_i$ and $\sigma_t$ in the *full* experiment was analyzed. This was done for both the FPMC and SB ROI, and compared to a theoretical model of noise sources similar to that of Krueger et al. (25), assuming that:

$$\sigma_{t,full} = \sqrt{\sigma_{ph}^2 + \sigma_{i,full}^2} \quad [3]$$

with $\sigma_{t,full}$ and $\sigma_{i,full}$ the temporal and intrinsic SD, respectively, in the *full* *k*-space data, and $\sigma_{ph}$ representing the contribution of physiological noise. For a given bandwidth and spatial resolution, the application of rate-*R* SENSE leads to an *R*-fold decrease in signal intensity and a $\sqrt{R}$-fold decrease in intrinsic noise in the acquired data. It is therefore expected to lead to an increased relative temporal SD, $\sigma_{t,SENSE}$, according to:

$$\sigma_{t,SENSE} = \sqrt{\sigma_{ph}^2 + (g \cdot \sqrt{R} \cdot \sigma_{i,full})^2}. \quad [4]$$

The increase in $\sigma_t$ is a function of *g*, *R*, and the relative contribution of $\sigma_i$ only:

$$\frac{\sigma_{t,SENSE}}{\sigma_{t,full}} = \sqrt{1 + (g^2R - 1) \cdot \left(\frac{\sigma_{i,full}}{\sigma_{t,full}}\right)^2}. \quad [5]$$

## RESULTS

All data acquired in the fMRI runs, with and without SENSE, showed significant activation in the FPMC area. Table 1 shows an overview of the calculated average *t*-values for *full*, *syn-alt*, *syn-odd*, *SENSE-alt*, and *SENSE-odd* fMRI data. Averaged over all subjects, *t*-scores obtained with *SENSE-alt* and *SENSE-odd* were 14% and 21% lower, respectively, than those acquired with *full*. Of these two, only the reduction observed with *SENSE-odd* was significant ($P$ = 0.02 for *SENSE-odd*, $P$ = 0.13 for *SENSE-alt*). The reduction in *t*-scores with *SENSE-alt* was significantly ($P$ = 0.005) less than 34%, which is the loss that would be predicted based on the $g \cdot \sqrt{R}$ reduction in image SNR (last column in Table 1). Performance of *SENSE-odd* was not significantly different from the $g \cdot \sqrt{R}$-based estimate ($P$ = 0.06). There was no significant difference in *t*-scores between *SENSE-alt* and *syn-alt* ($P$ = 0.34), or between *SENSE-odd* and *syn-odd* ($P$ = 0.93). Both *syn-alt* and *syn-odd* showed a significant 21% loss in *t*-score compared to *full* ($P$ = 0.0003 for *syn-alt*, $P$ = 0.00003 for *syn-odd*), a loss that was significantly less than the loss predicted based on $g \cdot \sqrt{R}$ reduction in image SNR ($P$ = 0.0009 for *syn-alt*, $P$ = 0.01 for *syn-odd*).

Analysis with the smaller FMPC2 resulted in overall higher *t*-scores, as expected when using more stringent criteria for selection of the activation threshold. On the other hand, similar relative trends between SENSE data and full-FOV data were observed, with *SENSE-alt* and *SENSE-odd* showing, respectively, 13% and 20% lower *t*-scores compared to *full* ($P$ = 0.08 and $P$ = 0.006, respectively).

The addition of a saw-tooth function to fMRI data analysis did not show an effect on the results. In the cases of *odd* and *full* data, the saw-tooth function was at noise level and showed no structure. Only in the case of *alt* data was a clear pattern observed (results not shown).

Table 2 summarizes *g*-, $\sigma_t$-, and $\sigma_i$-values, averaged over all subjects. Averages were computed over the FPMC, FPMC2, and SB ROIs. To obtain an indication of the extent of overlap (aliasing) in both FPMC and SB in the undersampled data (prior to SENSE reconstruction) the full-FOV data were used to predict the extent of potential aliasing. Voxels with alias intensity of more than 5% of the maximal intensity were considered to have overlap. This constituted 78.5% of FPMC voxels, 77.3% of FPMC2 voxels,

Table 1
Average *t*-Score in Primary Motor Cortex (FPMC) for Conventional and Two Rate 2 SENSE EPI Acquisition Schemes

| Volunteer | *t*-Score full | *t*-Score syn-alt | *t*-Score syn-odd | *t*-Score alt | *t*-Score odd | *t*-Score full/($g \cdot \sqrt{2}$) |
|---|---|---|---|---|---|---|
| 1 | 9.31 | 7.22 | 7.47 | 5.95 | 6.41 | 5.40 |
| 2 | 11.28 | 7.99 | 8.82 | 7.25 | 6.46 | 7.06 |
| 3 | 6.18 | 4.67 | 4.27 | 6.73 | 4.72 | 3.99 |
| 4 | 7.50 | 6.16 | 6.74 | 7.53 | 5.83 | 5.12 |
| 5 | 6.26 | 5.07 | 4.32 | 7.39 | 4.43 | 4.92 |
| 6 | 7.75 | 6.51 | 6.44 | 7.82 | 7.99 | 5.15 |
| 7 | 9.09 | 7.88 | 7.59 | 6.75 | 7.42 | 6.34 |
| 8 | 7.22 | 5.67 | 5.65 | 5.92 | 7.66 | 4.90 |
| Average (SD) | 8.07 (1.73) | 6.40 (1.24) | 6.41 (1.60) | 6.92 (0.71) | 6.37 (1.32) | 5.36 (0.94) |
| Average (SD) FPMC2 | 12.16 (1.80) | 9.99 (1.01) | 9.99 (1.42) | 10.55 (1.31) | 9.73 (1.17) | 8.07 (0.99) |

FPMC2 values were determined over a sub-region of FPMC.

and 44.0% of SB voxels. SENSE data showed an average $\sigma_t$-increase of 33% in FPMC when compared to *full* ($P = 0.004$), somewhat larger than the decrease in *t*-values. In the SB ROI the average $\sigma_t$-increase was on average 23% ($P = 0.003$), and in FPMC2 the average increase was 32% ($P = 0.006$). For *full*, $\sigma_i$-values were on average 38%, 47%, and 24% lower than $\sigma_t$ for the FPMC, FPMC2, and SB ROIs, respectively ($P = 0.00005$ for FPMC, $P = 0.00006$ for FPMC2, and $P = 0.03$ for SB).

Figure 3a–d shows scatter-plots of the $\sigma_t$-increase observed with SENSE as a function of the relative contribution of intrinsic noise ($\sigma_i$) to $\sigma_{t,full}$. This contribution was calculated from full-FOV and SENSE data using Eq. [5]. In Fig. 3a, the $\sigma_{t,SENSE}/\sigma_{t,full}$ ratio for all pixels in FPMC for *syn-alt* and *syn-odd* data from all volunteers is plotted as a function of the $\sigma_{i,full}/\sigma_{t,full}$ ratio, together with the theoretical curve (solid line) based on Eq. [5]. Figure 3b shows similar data for *SENSE-alt* and *SENSE-odd* experimental data. For the *syn-alt* and *syn-odd* data (Fig. 3a), 86% of the temporal variance ($\sigma_t^2$) can be explained by the model based on Eq. [5]. For *SENSE-alt* and *SENSE-odd* (Fig. 3b), 70% of $\sigma_t^2$ can be explained by this model. The increased deviation in Fig. 3b is possibly due to the fact that data of two separate experiments (SENSE and *full*), with potentially different levels of physiological noise, were used to calculate the plot. A more obvious correlation between measured and calculated $\sigma_{t,SENSE}/\sigma_{t,full}$ ratios is found when larger brain areas are analyzed within the same subject. An example of this is given in Fig. 3c and d, wherein SDs are plotted on a pixel-by-pixel basis for the entire SB ROI. Due to the strongly varying $\sigma_i$ levels across the brain, a result of spatially varying coil sensitivity, data points cover a larger range on the $\sigma_i/\sigma_t$-axis.

## DISCUSSION

The experiments described are a quantitative characterization of SENSE for single-shot BOLD fMRI. They illustrate the feasibility of using EPI-SENSE for fMRI with a reduced acquisition matrix.

The application of SENSE to reduce geometric distortions and blurring in EPI fMRI showed that image acquisition times as short as 12.4 ms are feasible for a nominal in-plane resolution of 3.4 mm. This led to a sensitivity of geometric distortions of only 43 $\mu m \cdot Hz^{-1}$, which would require impractical slew rates of 600 $T \cdot m^{-1} \cdot s^{-1}$ with full-FOV acquisition. Compared to full-FOV acquisition, the shorter acquisition window with SENSE resulted in an on average 34% increase in $\sigma_t$ and an 18% reduction in *t*-score for the two implemented versions of SENSE. This suggests that the SNR penalty incurred with SENSE does not necessarily lead to an equal loss in fMRI sensitivity.

No significant differences in performance of the *alt* and *odd* data were found, which indicates that adequate coil sensitivity maps can be derived from a limited number of volumes. On the other hand, the potentially increased temporal stability of *odd* data was not evident from the results. The possible temporal fluctuation in *alt* was accounted for through an additional saw-tooth fit function in fMRI analysis. This additional fit function potentially affects the observed *t*-scores, e.g., by artificially reducing background signal fluctuation. The fit function was there-

Table 2
Average Relative Intrinsic ($\sigma_i$) and Temporal ($\sigma_t$) Standard Deviations (%) for Primary Motor Cortex (FPMC and FPMC2) and Entire Superior Brain (SB)

| ROI | $g_{max}$ | $g_{avg}$ | $\sigma_i$ | $\sigma_{t,full}$ | $\sigma_{t,syn\text{-}alt}$ | $\sigma_{t,syn\text{-}odd}$ | $\sigma_{t,alt}$ | $\sigma_{t,odd}$ | $\sigma_{t,full} \cdot (g \cdot \sqrt{2})$ |
|---|---|---|---|---|---|---|---|---|---|
| FPMC | 1.32 | 1.09 | 0.56 | 0.91 | 1.10 | 1.09 | 1.18 | 1.25 | 1.39 |
| (SD) | (0.37) | (0.08) | (0.06) | (0.13) | (0.13) | (0.15) | (0.20) | (0.27) | (0.18) |
| FPMC2 | 1.22 | 1.08 | 0.53 | 0.98 | 1.15 | 1.15 | 1.26 | 1.33 | 1.50 |
| (SD) | (0.33) | (0.07) | (0.06) | (0.16) | (0.16) | (0.18) | (0.27) | (0.28) | (0.23) |
| SB | 2.19 | 1.06 | 0.79 | 1.04 | 1.27 | 1.24 | 1.26 | 1.29 | 1.55 |
| (SD) | (0.56) | (0.02) | (0.19) | (0.09) | (0.11) | (0.08) | (0.14) | (0.16) | (0.12) |

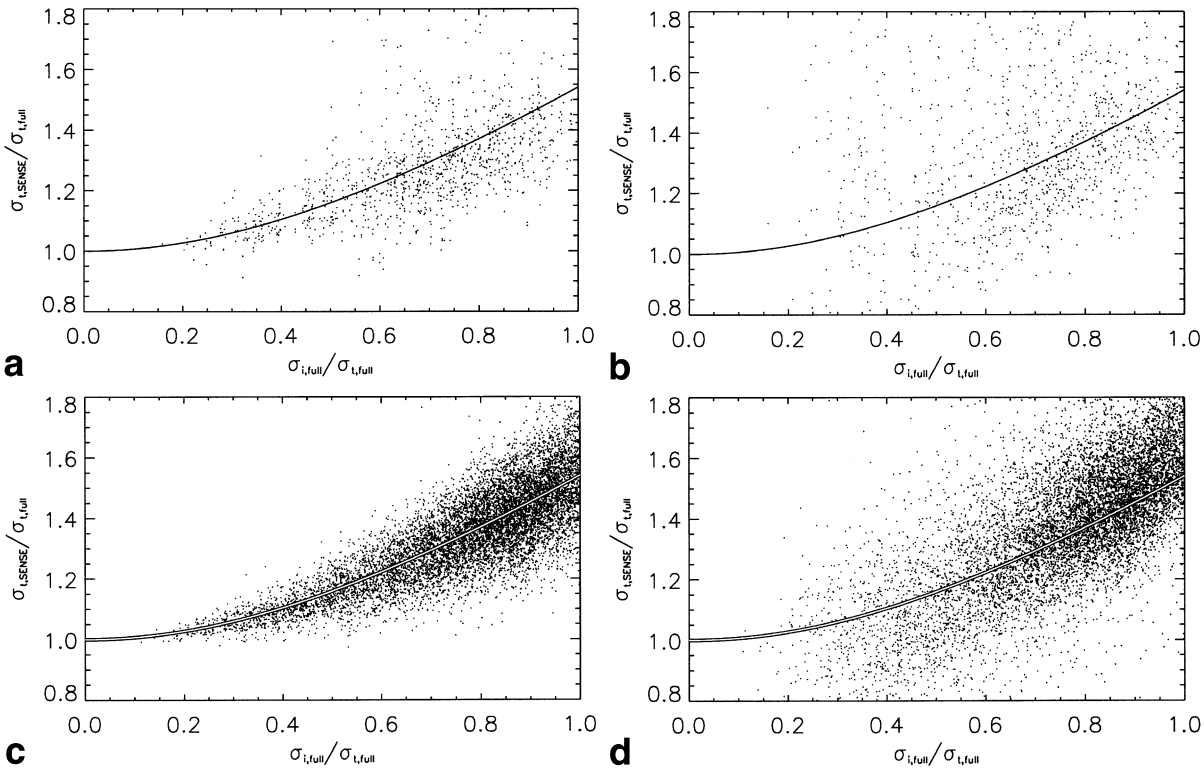


FIG. 3. Decrease in temporal stability with application of SENSE for reduction in EPI read-out duration. The ratio $\sigma_{t,SENSE}/\sigma_{t,full}$, temporal SD in SENSE and full-FOV data, is plotted against the contribution of intrinsic noise ($\sigma_{i,full}$) to the overall temporal stability in the full-FOV data ($\sigma_{t,full}$). The solid line is the theoretical curve based on Eq. [5]. In **a**, the results obtained on a pixel-by-pixel basis using both *syn-alt* and *syn-odd* data are shown. All voxels within FPMC for all the volunteers are plotted. A similar plot for *SENSE-alt* and *SENSE-odd* data is shown in **b**. Part **c** shows such data for all *syn-alt* pixels in SB for one of the volunteers; **d** shows the corresponding *SENSE-alt* data for the same volunteer.

fore also used in the analysis of *full* and *odd* data, on which it would have a similar filtering effect.

It is expected that the reduction in *t*-scores observed with shortening of the image acquisition window through SENSE will be smaller when the relative contribution of $\sigma_i$ is reduced (i.e., noise is dominated by physiological fluctuations). This can be effectuated by changing the experimental conditions, e.g., increasing the slice thickness, going to higher magnetic field strength, reducing the spatial resolution, lengthening the acquisition window, or shortening the TE.

One shortcoming of the current study is that ROI selection for sensitivity comparison was based on the functional data itself, which potentially generates a selection bias. A better strategy would be to acquire additional functional data, from which an unbiased ROI can be selected. Although *t*-scores in the FPMC2 ROI were significantly higher than the *t*-scores averaged over FPMC, relative *t*-score reduction in SENSE vs. *full* was marginally smaller (not significant) in FPMC2, an indication of the minimal effect of the selection bias in both ROIs. Although not directly evident from the results, the shortened data acquisition windows obtained with the SENSE application described above have other potentially important advantages. In the experiments described above, magnetic field uniformity was relatively good due to the particular location of the slices and the relatively low magnetic field. In fMRI experiments in the presence of strong magnetic susceptibility, e.g., in lower (more inferior) brain areas or at higher magnetic field, effects of background $T_2^*$ on image quality will be more significant, and the improvement with SENSE is expected to be more apparent. In addition, under these conditions, the shortened acquisition window is also expected to provide for improved BOLD sensitivity, since maximal BOLD effect is achieved at TE = $T_2^*$. The results presented here should therefore serve primarily as an indication of the issues involved with application of SENSE.

One way to reduce the sensitivity losses with SENSE, while retaining the advantage of reduced geometric distortions, is to acquire multiple SENSE EPI read-outs. The individual read-outs could be averaged after reconstruction, or $T_2^*$ fitting over the echoes could be performed to improve *t*-scores (26). Alternatively, one or more read-outs could be dedicated for use as a navigator to correct for motion-related intensity variations.

Another application that is currently under investigation is the use of SENSE to reduce gradient slew rates at constant resolution and constant EPI acquisition window duration. Preliminary results show that, on average, a 11.3 dB(A) reduction in sound pressure levels can be

achieved with rate-2 SENSE, while no significant change in *t*-scores was found (12).

Alternatively, the reduced data acquisition in parallel imaging can be exploited to increase spatial resolution for a given data acquisition window (27).

With the current coil design, the use of higher SENSE acceleration rates was prohibitive due to the strong increase in *g*-factors beyond an acceleration rate of 2. In addition, anatomical coverage was limited to the superior brain. Preliminary measurements with SENSE-optimized coil designs with a large number of channels and whole-brain coverage (21) show lower *g*-values. Such designs are expected to allow fMRI with acceleration rates of 3 or higher.

## CONCLUSIONS

The present experiments demonstrate the use of SENSE (and TSENSE) for reduction of the data acquisition window. SENSE-related sensitivity losses in fMRI are smaller than losses in image SNR, and depend on the relative contributions of thermal and physiological noise sources. It is expected that SENSE will have major applications in BOLD fMRI, particularly when used at high magnetic fields and with dedicated receive coils.

## ACKNOWLEDGMENTS

The authors thank Patrick Ledden of Nova Medical Inc. for supply of hardware and for helpful discussions.

## APPENDIX A

### Noise in SENSE Data

Coil pixel values $\mathbf{P}$ are a function of the signal $b$ that originates from the object, coil sensitivity profiles $\mathbf{S}$, and a combination of physiological noise ($\boldsymbol{\epsilon}_{ph}$) and intrinsic sample noise ($\boldsymbol{\epsilon}_i$) errors:

$$\mathbf{P} = \mathbf{S}b + \mathbf{S}\boldsymbol{\varepsilon}_{ph} + \boldsymbol{\varepsilon}_i. \quad [A1]$$

With $\boldsymbol{\epsilon} = \mathbf{S}\boldsymbol{\epsilon}_{ph} + \boldsymbol{\epsilon}_i$, the covariance estimate of the image intensity, $I_c$ (see Eq. [1]), becomes:

$$\begin{aligned}\mathrm{cov}(I_c) &= \mathrm{E}\{[(\mathbf{S}^H\boldsymbol{\Psi}^{-1}\mathbf{S})^{-1}(\mathbf{S}^H\boldsymbol{\Psi}^{-1}\boldsymbol{\varepsilon})][(\mathbf{S}^H\boldsymbol{\Psi}^{-1}\mathbf{S})^{-1}(\mathbf{S}^H\boldsymbol{\Psi}^{-1}\boldsymbol{\varepsilon})]^H\} \\ &= \mathrm{E}\{(\mathbf{S}^H\boldsymbol{\Psi}^{-1}\mathbf{S})^{-1}\mathbf{S}^H\boldsymbol{\Psi}^{-1}\boldsymbol{\varepsilon}\boldsymbol{\varepsilon}^H\boldsymbol{\Psi}^{-1}\mathbf{S}(\mathbf{S}^H\boldsymbol{\Psi}^{-1}\mathbf{S})^{-1}\}. \quad [A2]\end{aligned}$$

Since

$$\begin{aligned}\boldsymbol{\varepsilon}\boldsymbol{\varepsilon}^H &= (\boldsymbol{\varepsilon}_i + \mathbf{S}\boldsymbol{\varepsilon}_{ph})(\boldsymbol{\varepsilon}_i + \mathbf{S}\boldsymbol{\varepsilon}_{ph})^H \\ &= \boldsymbol{\varepsilon}_i\boldsymbol{\varepsilon}_i^H + \boldsymbol{\varepsilon}_i(\mathbf{S}\boldsymbol{\varepsilon}_{ph})^H + \mathbf{S}\boldsymbol{\varepsilon}_{ph}\boldsymbol{\varepsilon}_i^H + \mathbf{S}\boldsymbol{\varepsilon}_{ph}(\mathbf{S}\boldsymbol{\varepsilon}_{ph})^H \quad [A3]\end{aligned}$$

and $\mathrm{E}\{\boldsymbol{\epsilon}_i\,\boldsymbol{\epsilon}_i{}^{\mathrm{H}}\} = \boldsymbol{\Psi}$, $\mathrm{E}\{\boldsymbol{\epsilon}_i(\mathbf{S}\boldsymbol{\epsilon}_{ph})^{\mathrm{H}}\} = 0$ and $\mathrm{E}\{\mathbf{S}\boldsymbol{\epsilon}_{ph}\boldsymbol{\epsilon}_i{}^{\mathrm{H}}\} = 0$ (i.e. no correlation between $\boldsymbol{\epsilon}_i$ and $\boldsymbol{\epsilon}_{ph}$), this results in:

$$\begin{aligned}\mathrm{cov}(I_c) = \mathrm{E}\{&(\mathbf{S}^H\boldsymbol{\Psi}^{-1}\mathbf{S})^{-1}\mathbf{S}^H\boldsymbol{\Psi}^{-1} \\ &\times (\boldsymbol{\Psi} + \mathbf{S}\boldsymbol{\varepsilon}_{ph}\boldsymbol{\varepsilon}_{ph}^H\mathbf{S}^H)\boldsymbol{\Psi}^{-1}\mathbf{S}(\mathbf{S}^H\boldsymbol{\Psi}^{-1}\mathbf{S})^{-1}\}. \quad [A4]\end{aligned}$$

In the case in which noise is completely dominated by intrinsic noise ($\boldsymbol{\epsilon}_i$), this leads to:

$$\mathrm{cov}(I_c) = \mathrm{E}\{(\mathbf{S}^H\boldsymbol{\Psi}^{-1}\mathbf{S})^{-1}\} \quad [A5]$$

$$\begin{aligned}\frac{\sigma_{t,SENSE}}{\sigma_{t,full}} &= \frac{\sqrt{\mathrm{cov}(I_{c,SENSE})}}{\sqrt{\mathrm{cov}(I_{c,full})}} = \frac{\sqrt{(\mathbf{S}_{SENSE}^H\boldsymbol{\Psi}^{-1}\mathbf{S}_{SENSE})^{-1}_{q,q}}}{\sqrt{(\mathbf{S}_{full}^H\boldsymbol{\Psi}^{-1}\mathbf{S}_{full})^{-1}}} \\ &= \sqrt{(\mathbf{S}_{SENSE}^H\boldsymbol{\Psi}^{-1}\mathbf{S}_{SENSE})^{-1}_{q,q}\cdot(\mathbf{S}_{full}^H\boldsymbol{\Psi}^{-1}\mathbf{S}_{full})} = g\cdot\sqrt{R}. \quad [A6]\end{aligned}$$

Note that the *g*-factor (Eq. [2]), defined implicitly in Eq. [A6], corresponds to the sample noise-limited case without physiological noise contribution. The factor $R$ signal intensity difference between $\mathbf{S}_{SENSE}$ and $\mathbf{S}_{full}$ leads to the additional factor $\sqrt{R}$ in Eq. [A6]. The $(q,q)$-index indicates the use of diagonal matrix elements. In the other extreme, when noise is completely dominated by physiological noise ($\boldsymbol{\epsilon}_{ph}$), Eq. [A4] becomes:

$$\mathrm{cov}(I_c) = \mathrm{E}\{\boldsymbol{\varepsilon}_{\mathbf{ph}}\boldsymbol{\varepsilon}_{\mathbf{ph}}^H\} = \boldsymbol{\Psi}_{ph} \quad [A7]$$

and

$$\sigma_t = \frac{\sqrt{(\boldsymbol{\Psi}_{ph})_{q,q}}}{|I_c|} \quad [A8]$$

where $\boldsymbol{\Psi}_{ph}$ is the $R \times R$ physiological noise covariance matrix or correlation coefficient between corresponding pixels in the $R$ subimages ($\boldsymbol{\epsilon}_{ph}$ is an $R \times 1$ vector). Note that $\sigma_{ph}$ is not dependent on the SENSE rate, $R$, since perfect unmixing of the aliased pixels has been assumed. Thus, the SD $\sigma_{ph}$ is the same for SENSE and a comparable conventional experiment without loss in SNR due to either acceleration or matrix ill-conditioning (*g*-factor).

## APPENDIX B

### Calculation of Intrinsic Noise Level

To calculate relative intrinsic noise levels $\sigma_i$ (normalized by signal intensity), as used in the evaluation of the fMRI results, full-FOV data were used. First the combined noise variance $V_c$ was calculated from the noise covariance matrix and coil sensitivity profiles $\mathbf{S}$ of the individual coils, using Eq. [1]:

$$V_c = (\mathbf{S}^H\boldsymbol{\Psi}^{-1}\mathbf{S})^{-1}. \quad [B1]$$

Second, the relative intrinsic noise levels ($\sigma_i$), normalized to the temporal mean of signal intensity, were calculated on a pixel-by-pixel basis from:

$$\begin{aligned}\sigma_i = \frac{\sqrt{1/2\cdot V_c}}{|I_c|} &= \frac{\sqrt{1/2\cdot(\mathbf{S}^H\boldsymbol{\Psi}^{-1}\mathbf{S})^{-1}}}{|(\mathbf{S}^H\boldsymbol{\Psi}^{-1}\mathbf{S})^{-1}(\mathbf{S}^H\boldsymbol{\Psi}^{-1}\mathbf{P})|} \\ &= \frac{\sqrt{1/2\cdot(\mathbf{S}^H\boldsymbol{\Psi}^{-1}\mathbf{S})}}{|(\mathbf{S}^H\boldsymbol{\Psi}^{-1}\mathbf{P})|}. \quad [B2]\end{aligned}$$

The factor 1/2 in Eq. [B2] takes into account the effect that, in images with SNR $\gg 1$, only the noise component in-phase with the signal contributes to the variance (28). Due to the particular fashion in which the coil sensitivity profiles were derived (see Appendix C), which circumvented the need of a body coil reference image, **S** contained a phase and amplitude scale factor that is not uniform of the image. Although this fact was ignored in the derivation of Eq. [B2], it does not affect its validity, since it is insensitive to phase and amplitude factors in **S** that are shared between coils.

## APPENDIX C

### Calculation of Coil Sensitivity Profiles

The coil sensitivity **S**, required for coil combining using Eq. [1], was calculated from complex coil pixel values **P**, derived from full-FOV data by removing object phase and intensity contrast:

$$\mathbf{S} = \frac{\mathbf{P}}{Ae^{i\varphi_c}} \qquad [C1]$$

with

$$A = \sqrt{\mathbf{P}^H\mathbf{P}} \qquad [C2]$$

the root-sum-of-squares (RSS) combined pixel values, and

$$\varphi_c = \text{phase}\left[\sum_j |\mathbf{P}_j|\mathbf{P}_j e^{-i\varphi_{j,center}}\right] \qquad [C3]$$

the phase of the weighted combination of complex pixel values with weights calculated to optimize the signal at the object center. In Eq. [C3], the summation was performed over the coil elements, and $\varphi_{j,center}$ was the phase in the center of the object for coil *j*. This particular phase combination resulted in a low-noise estimate of the phase, $\varphi_c$. To minimize noise in the sensitivity maps, a $3 \times 3$ smoothing filter was applied to all voxels that were three or more voxels deep inside the object, as determined from an object mask generated by applying an intensity threshold to the RSS combined coil images. The smoothing was applied to the real and imaginary part of the data individually. Voxels closer to the edge were subjected to a second-order polynomial fit, using an $11 \times 11$ area centered on each voxel as the support region. As with the smoothing, fitting was performed on the real and imaginary parts of the data individually. The result of the fit was used to estimate the coil sensitivity in a 5-pixel-wide rim surrounding the mask. The additional sensitivity information was calculated to help avoid potential reconstruction problems in cases of significant object displacement in the time between acquisition of reference data and the actual experiment.

## APPENDIX D

### Determination of Noise Correlation

Noise correlation between coil channels was assessed using full-FOV MRI data, acquired on the same volunteer after completion of the fMRI runs, with the input to the RF amplifier blanked. The 2D noise covariance matrix $\boldsymbol{\Psi}$ was calculated:

$$\boldsymbol{\Psi}_{ij} = \frac{\sum_m \mathbf{P}_{i,m}\mathbf{P}^*_{j,m}}{\sqrt{\sum_m \mathbf{P}_{i,m}\mathbf{P}^*_{i,m} \cdot \sum_m \mathbf{P}_{j,m}\mathbf{P}^*_{j,m}}} \qquad [D1]$$

where $\mathbf{P}_{i,m}$ is the complex signal value from coil *i* in data point *m*.

## REFERENCES


1. Glover GH, Lee AT. Motion artifacts in fMRI—comparison of 2DFT with PR and spiral scan methods. Magn Reson Med 1995;33:624–635.
2. Yang YH, Glover GH, van Gelderen P, Pater AC, Mattay VS, Frank JA, Duyn JH. A comparison of fast MR scan techniques for cerebral activation studies at 1.5 Tesla. Magn Reson Med 1998;39:61–67.
3. Jesmanowicz A, Bandetini PA, Hyde JS. Single-shot half *k*-space high-resolution gradient-recalled EPI for fMRI at 3 Tesla. Magn Reson Med 1998;40:754–762.
4. Margosian P, Schmitt F, Purdy D. Faster MR imaging: imaging with half the data. Health Care Instrum 1986;1:195–197.
5. Hyde JS, Biswal BB, Jesmanowicz A. High resolution fMRI using multislice partial *k*-space GR-EPI with cubic voxels. Magn Reson Med 2001;46:114–125.
6. Hutchinson M, Raff U. Fast MRI data acquisition using multiple detectors. Magn Reson Med 1988;6:87–91.
7. Ra JB, Rim CY. Fast imaging using subencoding data sets from multiple detectors. Magn Reson Med 1993;30:142–145.
8. Sodickson DK, Manning WJ. Simultaneous acquisition of spatial harmonics (SMASH): fast imaging with radiofrequency coil arrays. Magn Reson Med 1997;38:591–603.
9. Pruessmann KP, Weiger M, Scheidegger MB, Boesinger P. SENSE: sensitivity encoding for fast MRI. Magn Reson Med 1999;42:952–962.
10. Roemer PB, Edelstein WA, Hayes CE, Souza SP, Mueller OM. The NMR phased array. Magn Reson Med 1990;16:192–225.
11. Bammer R, Keeling SL, Augustin M, Pruessmann KP, Wolf R, Stollberger R, Hartung HP, Fazekas F. Improved diffusion-weighted single-shot echo-planar imaging (EPI) in stroke using sensitivity encoding (SENSE). Magn Reson Med 2001;46:548–554.
12. de Zwart JA, van Gelderen P, Kellman P, Duyn JH. Reduction of gradient acoustic noise in MRI using SENSE-EPI. Neuroimage 2002;16:1151–1155.
13. Jakob PM, Griswold MA, Edelman RR, Manning WJ, Sodickson DK. Accelerated cardiac imaging using the SMASH technique. J Cardiovasc Magn Reson 1999;1:153–157.
14. Weiger M, Pruessmann KP, Boesinger P. Cardiac real-time imaging using SENSE. Magn Reson Med 2000;43:177–184.
15. Pruessmann KP, Weiger M, Boesinger P. Sensitivity encoded cardiac MRI. J Cardiovasc Magn Reson 2001;3:1–9.
16. Weiger M, Pruessmann KP, Kassner A, Roditi G, Lawton T, Reid A, Boesinger P. Contrast-enhanced 3D MRA using SENSE. J Magn Reson Imaging 2000;12:671–677.
17. Golay X, Pruessmann KP, Weiger M, Crelier GR, Folkers PJM, Kollias SS, Boesinger P. PRESTO-SENSE: an ultrafast whole-brain fMRI technique. Magn Reson Med 2000;43:779–786.
18. Larkman DJ, Hajnal JV, Herlihy AH, Coutts GA, Young IR, Ehnholm G. Use of multicoil arrays for separation of signal from multiple slices simultaneously excited. J Magn Reson Imaging 2001;13:313–317.
19. Jakob PM, Griswold MA, Edelman RR, Sodickson DK. AUTO-SMASH: a self-calibrating technique for SMASH imaging. MAGMA 1998;7:42–54.
20. Kellman P, Epstein FH, McVeigh ER. Adaptive sensitivity encoding incorporating temporal filtering (TSENSE). Magn Reson Med 2001;45:846–852.
21. de Zwart JA, Ledden P, van Gelderen P, Kellman P, Duyn JH. Design of a sensitivity optimized SENSE MRI receive coil for brain imaging. Magn Reson Med 2002;47:1218–1227.
22. Ledden PJ, Inati S. Four channel preamplifier decoupled phased array for brain imaging at 1.5T. In: Proceedings of the 9th Annual Meeting of Glasgow, Scotland, 2001. p 1117.

23. Bruder H, Fischer H, Reinfelder H-E, Schmitt F. Image reconstruction for echo planar imaging with nonequidistant *k*-space sampling. Magn Reson Med 1992;23:311–323.
24. Waldvogel D, van Gelderen P, Muellbacker W, Ziemann U, Immisch I, Hallett M. The relative metabolic demand of inhibition and excitation. Nature 2000;406:995–998.
25. Krueger G, Kastrup A, Glover GH. Neuroimaging at 1.5T and 3.0T: comparison of oxygenation sensitive magnetic resonance imaging. Magn Reson Med 2001;45:595–604.
26. Speck O, Hennig J. Functional imaging by $I_o$- and $T_2$* parameter mapping using multi-image EPI. Magn Reson Med 2001;40:243–248.
27. de Zwart JA, van Gelderen P, Kellman P, Duyn JH. Application of sensitivity-encoded EPI for BOLD fMRI. In: Proceedings of the Workshop on Minimum MR Data Acquisition Methods: Making More With Less, Marco Island, Florida, 2001. p 153–156.
28. Hayes CE, Roemer PB. Noise correlations in data simultaneously acquired from multiple surface coil arrays. Magn Reson Med 1990;16: 181–191.